Effects of three-dimensional coating interfaces on thermo-mechanical stresses within plasma spray thermal barrier coatings

KYAW, Si <http://orcid.org/0000-0001-8568-500X>, JONES, Arthur, JEPSON, Mark A.E., HYDE, Tom and THOMSON, Rachel C.

Published version

KYAW, Si, JONES, Arthur, JEPSON, Mark A.E., HYDE, Tom and THOMSON, Rachel C. (2017). Effects of three-dimensional coating interfaces on thermo-mechanical stresses within plasma spray thermal barrier coatings. Materials & Design, 125 (5), 189-204.

Effects of three-dimensional coating interfaces on thermo-mechanical stresses within plasma spray thermal barrier coatings

Si Kyaw[a], Arthur Jones[a], Mark A. E. Jepson[b], Tom Hyde[a], Rachel C. Thomson[b]

[a] Faculty of Engineering, The University of Nottingham
University Park, Nottingham, NG7 2RD, UK
[b]Department of Materials, Loughborough University,
Loughborough, LE11 3TU, UK

Abstract

It has been acknowledged that stresses within a thermal barrier coating (TBC) and its durability are significantly affected by the coating interfaces. This paper presents a finite element approach for stress analysis of the plasma sprayed TBC system, using three-dimensional (3D) coating interfaces. 3D co-ordinates of the coating surfaces were measured through 3D reconstruction of scanning electron microscope (SEM) images. These co-ordinates were post processed to reconstruct finite element models for use in stress analyses. A surface profile unit cell approach with appropriate boundary conditions was applied to reduce the problem size and hence computation time. It has been shown that for an identical aspect ratio of the coating interface, interfacial out-of-plane stresses for 3D models are around twice the values predicted using 2D models. Based on predicted stress development within the systems, possible crack development and failure mechanisms of the TBC systems can be predicted.

1 Introduction

Thermal barrier coating (TBC) systems are applied onto various superalloy and metal components e.g. gas turbine blades of an aircraft, diesel engine combustion chambers etc. One of the key functions of a TBC is to create a reduction in the substrate temperature by slowing the rate of thermal conduction of heat from a combustion reaction to the (cooled) substrate. This allows an increase in the combustion temperature which can lead to an increased efficiency. A TBC system typically consists of two applied layers: a metallic bond coat (BC), and a ceramic top-coat (TC). The TC is the outermost layer of the system and provides temperature reduction due to its low thermal conductivity, while the BC provides a structural link with the substrate. Coatings are applied using different methods and here only an air plasma sprayed (APS) system is considered. The method is more commonly used for components of land-based gas turbine engines. For this system, the surface roughness of the BC provides a mechanical bond to the TC and also influences its lifetime [1]. The BC is a mixture of β (NiAl), γ' (Ni3Al) and γ (Ni) phases in various proportions. At high temperature, the composition of the BC evolves either due to formation of a thermally grown oxide (TGO) at the TC/BC interface from oxygen diffusion [2] or due to interdiffusion at the substrate/BC interface [3, 4]. This variation in the BC compositions with service time can affect its mechanical properties significantly [5, 6].

Although the rough surface of the BC provides a mechanical bond to the TC, it can also cause out-of-plane stresses within the system as it undergoes thermal cycling. Early efforts to relate BC surface roughness and thermo-mechanical stresses within APS TBC systems have been carried out numerically in [7-9] where predictions were made using idealised 2D interfaces, based on micrographs of cross-sections of coating layers. Possible

reasons for these simple approaches are: inadequate computational power to run FE simulations of actual coating interface and, the difficulty involved with the characterisation of interface profiles from standalone coatings. Idealised interfaces not only fail to give an accurate representation of the actual geometry, but are, therefore, also likely to result in simulated TBC stresses which are insufficiently accurate for predictions of failure of the TBCs. Therefore, it is desirable to construct an FE unit cell to represent the actual surface geometry and hence to predict stress distributions within the TBC system accurately. A recent review [10] explores more generally the use of FE models for predicting TBC thermal behaviour and failure including the use of 3D models.

Nowadays, complex microstructural features can be measured by various advanced methods [11, 12]. Furthermore, computational tools (such as object oriented finite element or OOF2 [13]) transform micrograph images into FE meshes to be used for further FE analyses. The application of this method for stress analysis of the TBCs can be found in [14]. The work not only captures the roughness profile but also porous area within the coatings, which provides useful information to calculate the coating's thermal conductivity. Rezvani Rad, et al. [15] and Nayebpashaee, et al. [16] used a similar technique to identify the effect of realistic 2D roughness profiles on out-of-plane stresses under thermo-mechanical and thermal fatigue load conditions respectively. Measurements of 3D coating profiles were also used by Gupta et al. [17, 18] to construct 3D FE models and the resultant residual stresses were compared against results from 2D FE models. For similar aspect ratio of the interface, out-of-plane stresses predicted from 3D models are around half an order of magnitude higher than those predicted from 2D models under similar loading conditions. The results highlight the importance of 3D interface shape to the estimation of residual stresses within TBC systems. Work by Saucedo-Mora, et al. [19] considered the microstructural roughness and heterogeneity of the coating for damage development within coatings using multi-scale FE model. The work not only demonstrated the effects of surface roughness on stress profiles, but also the influence of microstructural features on Young's modulus and damage within coatings.

Despite current abilities to incorporate complex coating interfaces into FE analyses, there are still many shortcomings among the models presented in the previous paragraph. The models in [15, 18] ignore oxidation of the BC completely, yet this is very important due to the non-planar nature of the interface shape. When a BC oxidises, directional oxide growth strains and subsequent stresses build up within the system in a manner dependent on interface geometry. Nayebpashaee, et al. [16] considered oxidation by applying an empirical swelling strain to an initial oxide later without taking account of continuous consumption of the BC due to oxidation. Gupta et al. [17] calculated the oxide layer thickness based on the diffusion at the BC interfaces. However, the simulation only used a linear elastic material model to investigate the mismatch stress due to change in temperature. The model also ignored the stress build up and redistribution due to creep of coatings during the steady state. To address the aforementioned shortcomings, this paper reports an FE model that has been produced which describes the effect of stresses within a coating system of 3D microscopic features, extracted from 3D analysis of real coating interfaces. Appropriate boundary conditions presented by Li et al. [20] were applied to reduce the size of the surface profile unit cell and hence its computation time. Changes in material properties of the coating due to oxidation and sintering have also been incorporated to fully describe the changes taking place during service. A simple case study has been carried out using simplified 2D and 3D TGO interface idealisations with identical aspect ratios (ratio of amplitude to wavelength). Subsequently, two FE unit cells based on 3D microscopic features of the BC were built to carry out analysis of stress distribution and relate them to the failure of the TBC.

This work fits into the present Journal's priority area [21] of the analysis, structure, morphology and role of interfaces in the context of multi-physics phenomena, specifically by describing the influences of manufacturing-related interface geometry on the development of stresses and cracks due to thermo-mechanical and oxidation effects. This paper documents the development of a theoretical model of interface stress with the use of experimental data of interface geometry which can be used in the design of future turbine blade coatings.

2 Roughness modelling

2.1 Capturing and post processing of TGO surface profiles

Cross-sections of TBC systems are traditionally imaged using a scanning electron microscope (SEM). Nevertheless, as these interfaces are often view in cross-section, their interface roughness and surface profile data measured using this method might not always represent the actual aspect ratio. The concept can be appreciated through the examination of Fig. 1~~Fig. 1~~ where three different sectioning paths of an idealised surface with identical aspect ratio throughout its surface could form radically different cross-section profiles. To avoid this, 3D images of the coating interface were captured for the current work.

The specimen used for the capture of the TGO surface profile was composed of a Ni22Co17Cr12Al0.6Y (Wt.%) BC with an APS TBC which was isothermally heated to a temperature of 940°C for 500 h. In order to view the TGO / BC interface, the BC was dissolved in hydrochloric acid (36%) for 36h at ambient temperature to reveal the surface of the oxide interface as used by Sohn et al. [22]. To produce a 3D representation of the TGO / BC interface, secondary electron images were collected using a Cambridge 360 Stereoscan SEM at a number of tilt angles and analysed using Alicona Mex 3D. The x-y-z coordinates of the measured surface profile were then saved in ASCII format and post-processed using 'Fogale Nanotech Profilometry Software' (FNPS) [23]. In order to approximate a TGO layer of constant thickness within the FE model, it was assumed that both TGO interfaces (i.e. TBC / TGO and TGO / BC) follow identical geometries.

The measured TGO surface coordinates in ASCII format were imported into FNPS, and the roughness profile (short wavelength undulations) and waviness (longer wavelength than the roughness profile) of the interface were separated using a standardised Gaussian filtering method (ISO 11562) [24]. The weight function of the filter (S(x)) is given by Eq (1)~~(1)~~ [25]. The mean line of the raw data was obtained by convolving it with the weighting function. The roughness and waviness profiles were separated by subtracting the mean line from the raw profile. The transfer function was obtained by performing a Fourier transform of the continuous function S(x) as shown in Eq (2)~~(2)~~ [26].

$$S(x)=\frac{1}{\alpha\lambda_c}\exp\left(-\pi\left(\frac{x}{\alpha\lambda_c}\right)^2\right) \tag{1}$$

$$Sf(\lambda)=\int_{-\infty}^{\infty}S(x)\exp(i\lambda x)\,dx=\exp\left(-\pi\left(\frac{\alpha\lambda_c}{\lambda}\right)^2\right) \tag{2}$$

where $\alpha=\sqrt{\frac{\ln 2}{\pi}}$, x is the distance from the origin of the weight function, λ_c is the cut-off for longer wavelength roughness and λ is the actual wavelength of different waves from the raw surface profile.

As observed from Eq (1)~~(1)~~ and (2)~~(2)~~, the filtering process is mainly controlled by the choice of cut-off wavelength (λ_c). There are several uncertainties in choosing the cut-off wavelength as it has not only to be short enough to separate waviness profiles, but also long enough to give a meaningful roughness profile. A longer cut-off wavelength creates a smoother roughness profile and vice versa. Since there is no definite standard for the cut-off wavelength, the choice of the wavelength is entirely dependent on the sizes of the asperities, on which analyses are to be performed. In the present work, a cut-off wavelength of 25 µm was used to separate the microscopic roughness features from large protuberances of isolated BC "splats". The height contour plots of the roughness and waviness profiles of the TGO/BC interface within the sample area of 200 µm x 140 µm are depicted in Fig.2~~Fig.2~~.

Formatted: Font: 12 pt, Not Bold

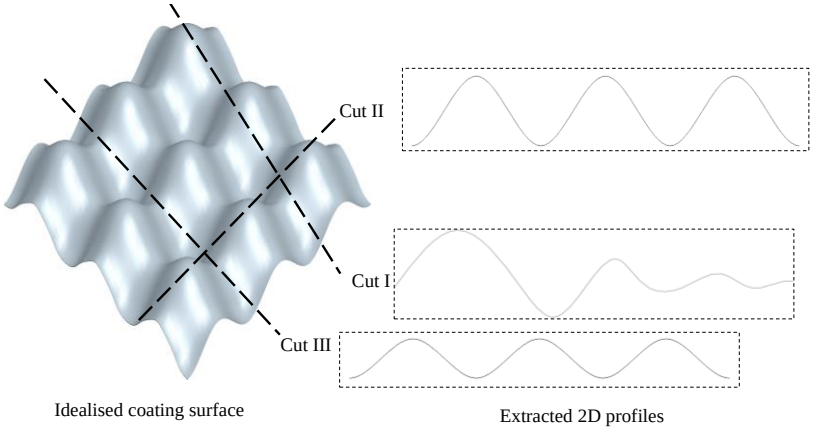

Fig. 1: Possible coating roughness profiles that could be extracted from different 2D cross-sectional micrographs of the coating surface with perfectly periodic asperities

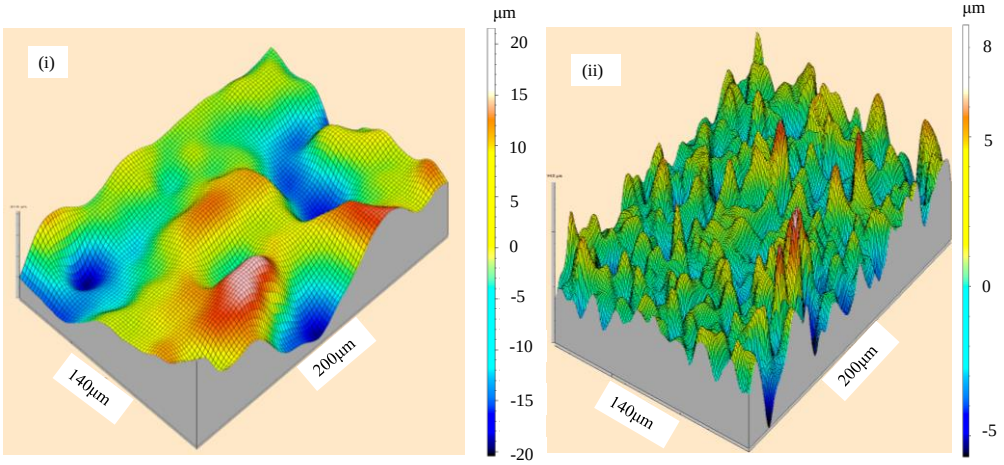

Fig.2: (i) Waviness and (ii) roughness profiles of the TGO/NiCoCrAlY BC interface with cut off wavelength (λ_c) = 25µm (profiles were generated using FNPS). Vertical axes and scales show out-of-plane profile in µm (height exaggerated)

2.2 Types of interface geometries

Three types of interface geometries were chosen for the various case studies. They are listed in Table 1~~Table 1~~.

Table 1: Geometries used in the current work and specimen from which they are extracted

Interface geometries	Detailed description	Specimen
(i)	A profile cell measured from SEM micrographs of 2D cross-sections	A range of TBC systems [5]
(ii)	A surface profile cell, extracted from 3D coating roughness measurements as shown in Fig.2~~Fig.2~~ (ii)	NiCoCrAlY specimen that had been heat treated at 940˚C for 500h (as described in Section 2)
(iii)	A surface profile cell, which represents the protuberance of a BC splat, whose wavelength is larger than the roughness sampling length (Extracted from Fig.2~~Fig.2~~ (i))	NiCoCrAlY specimen that had been heat treated at 940˚C for 500h (as described in Section 2)

Formatted: Font: 12 pt, Not Bold

Formatted: Font: 12 pt, Not Bold

Firstly, the interface geometry with amplitude (A) of 6 µm and wavelength (L) of 48 µm (denoted as A6-L48), as used in previous studies [5, 6], was used for the axisymmetric and 3D unit cell models as shown in Fig.3~~Fig.3~~ (i) & (ii). The thermo-mechanical stresses were simulated for these models at 20°C after aging for 900 h at 1000°C.

Formatted: Font: Not Bold

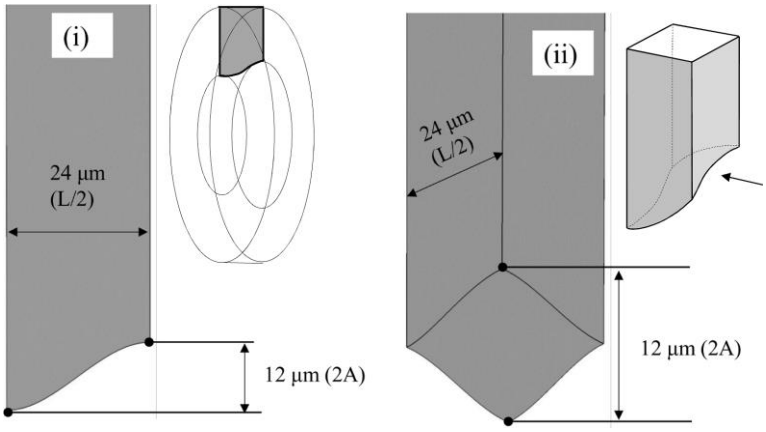

Fig.3: (i) Axisymmetric unit cell (L= 48µm, A = 6µm) (ii) Comparable 3D unit cell of TBC (Geometry set i). Insets show relationships of main views to 3D geometry

It is assumed that the features of a realistic rough interface, such as that shown in Fig.2~~Fig.2~~, can be broken down into three undulation components at different scales, known respectively as form, waviness and roughness. In order to investigate the relative effects of these, each of these was modelled separately since the overall problem involving all three scales would have been too large to model realistically within a single FE unit cell that includes all of these geometric features. Accordingly, separate unit cells were constructed to represent the roughness and waviness, with the form being included in the overall

Formatted: Font: 12 pt, Not Bold

axisymmetric or cylindrical geometry of the unit cell. Additionally, it is assumed that the tangential slopes are zero along the symmetry and the periodicity planes of the unit cells due to limitations imposed by the boundary conditions for a 3D unit cell (Section 3). This assumption allows the modelling of only a quarter of each microscopic feature.

An asperity extracted from the roughness profile of Fig.2~~Fig.2~~ (ii) is similar to the idealised 3D interface shown in Fig.3~~Fig.3~~ (ii). However, the aspect ratios of the interface for two in-plane directions were different as the actual peaks and troughs of the coating's interface were elliptical as shown in Fig.4~~Fig.4~~ (ii). A and L of the asperity are 3.3 µm and 22.5 µm respectively. It was assumed that the coating was covered with periodic features of the represented asperity as shown in Fig.4~~Fig.4~~ (iii). The substrate curvature for this specimen was 6.2 mm in this case and was incorporated with the unit cell as in [6].

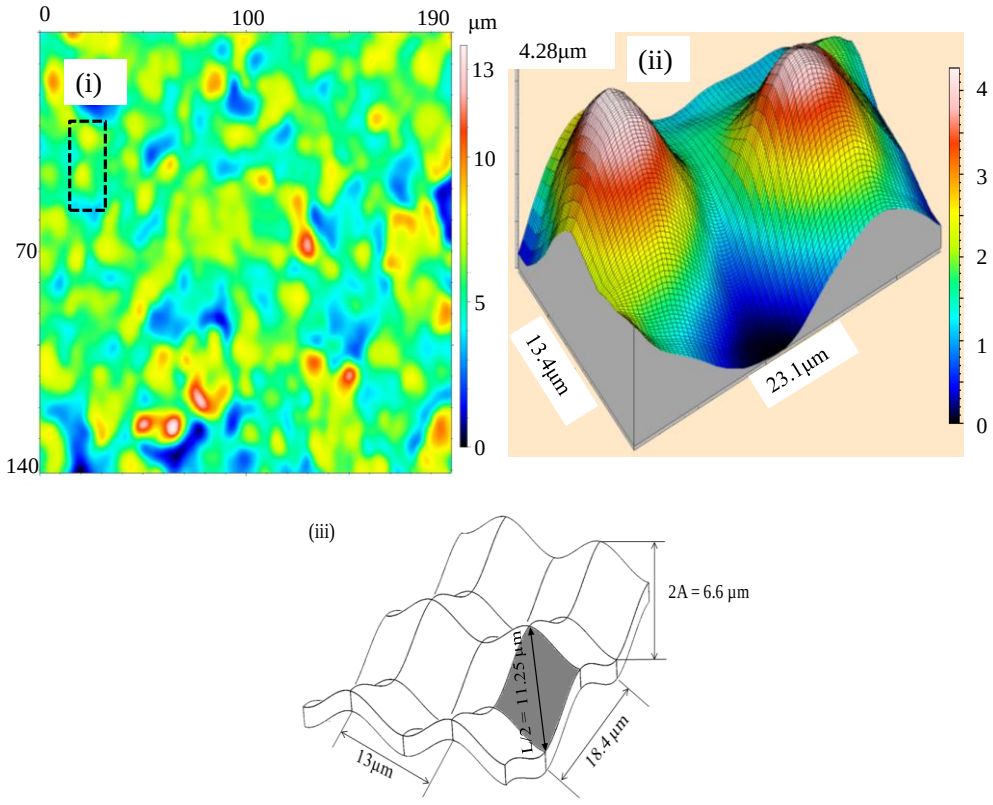

Fig.4: i) Surface contour plot of roughness profile and ii) 3D view of extracted asperity using FNPS (NiCoCrAlY system after 500h of heat treatment at 940°C) iii) Representative coating roughness modelled using a repeating unit cell (Geometry set ii) Vertical axis in ii), colour contours and scales show out-of-plane profile in µm (height exaggerated in ii))

As shown in Fig.5~~Fig.5~~, pits with depths significantly larger than those of the roughness asperities can be observed at the surface of the TGO. This feature will hereafter be referred to as an 'oxide loop'. A profile of an oxide loop formed after 500 h of heat treatment at 940°C was extracted from the 3D data of the TGO / BC surface. The length and width of the elliptical oxide loop were 32 µm and 24 µm respectively, and the depth was 15 µm. Because of the extreme aspect ratio of the oxide loop features, the form of the substrate was

Formatted: Font: 12 pt, Not Bold
Formatted: Font: Not Bold
Formatted: Font: 12 pt, Not Bold
Formatted: Font: 12 pt, Not Bold
Formatted: Font: Not Bold

assumed to have no significant effect upon the local stress field compared to that of the oxide loop. Therefore, the substrate was modelled as having zero curvature in either direction.

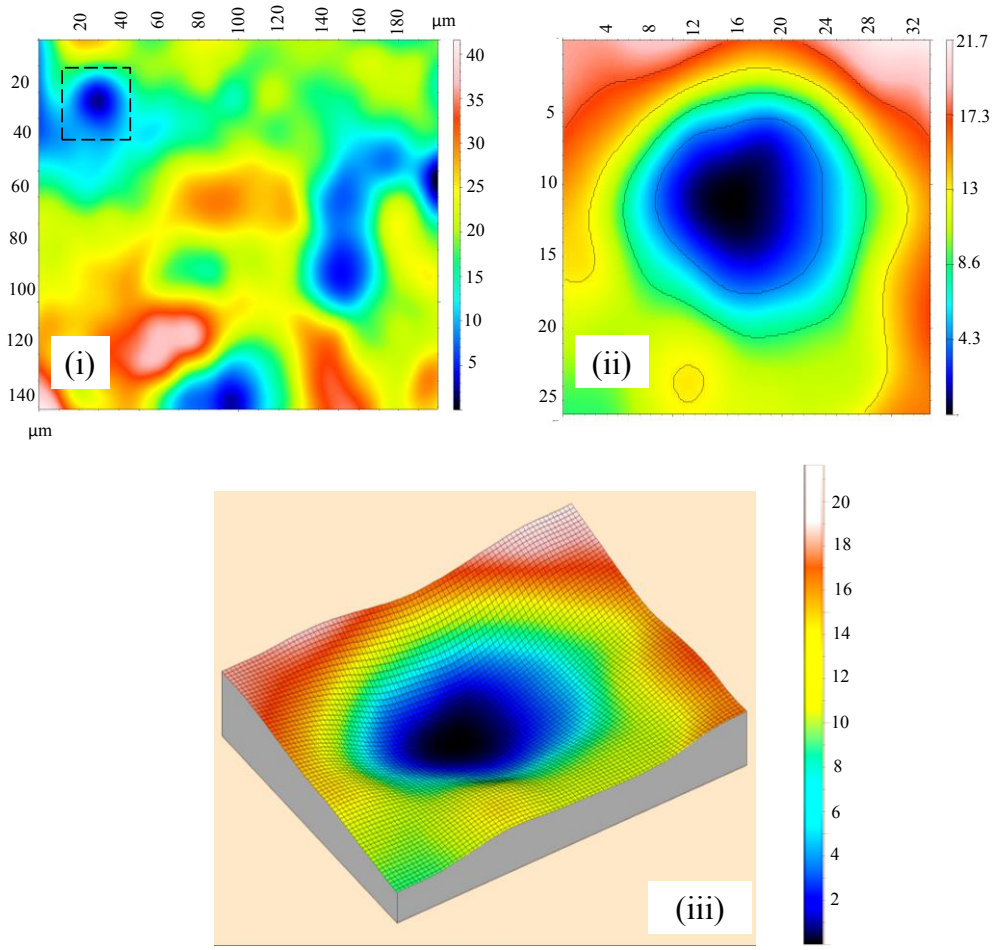

Fig.5: (i) Waviness profile at the surface of the TGO from NiCoCrAlY-APS TBC system, which has been heat treated at 940°C for 500h; oxide loop feature shown in dotted line is shown in detail in (ii) and (iii) Vertical axis in iii), colour contours and scales show out-of-plane profile in µm (profile height not to scale in iii))

3 Boundary conditions for microscopic features with cylindrical and longitudinal periodicities

In order to make the finite element simulation computationally efficient, the interface features identified in Section 2.2~~2.1~~ are idealised into an infinitely-repeating form and appropriate boundary conditions are applied. In the past, it has been assumed [5, 6, 27, 28] that the BC/TGO interface has a 2D shape with periodicity either in the circumferential

direction (with wavelength $2r\alpha$) or in the longitudinal direction (with wavelength $2b$) as shown in Fig.6~~Fig.6~~ (i & ii). Here, an idealised 3D model with periodicity in both circumferential and longitudinal directions can be modelled using a unit cell contained within the domain shown in Eq (3)~~(3)~~ [20] and having the repeating pattern shown in Fig.7~~Fig.7~~.

$$\begin{aligned} -b \le x \le b \\ 0 \le r \le R \\ -\alpha \le \theta \le \alpha \end{aligned} \qquad (3)$$

where x, r, and θ are longitudinal, radial and circumferential coordinates of the cylindrical coordinate system (CSYS), respectively.

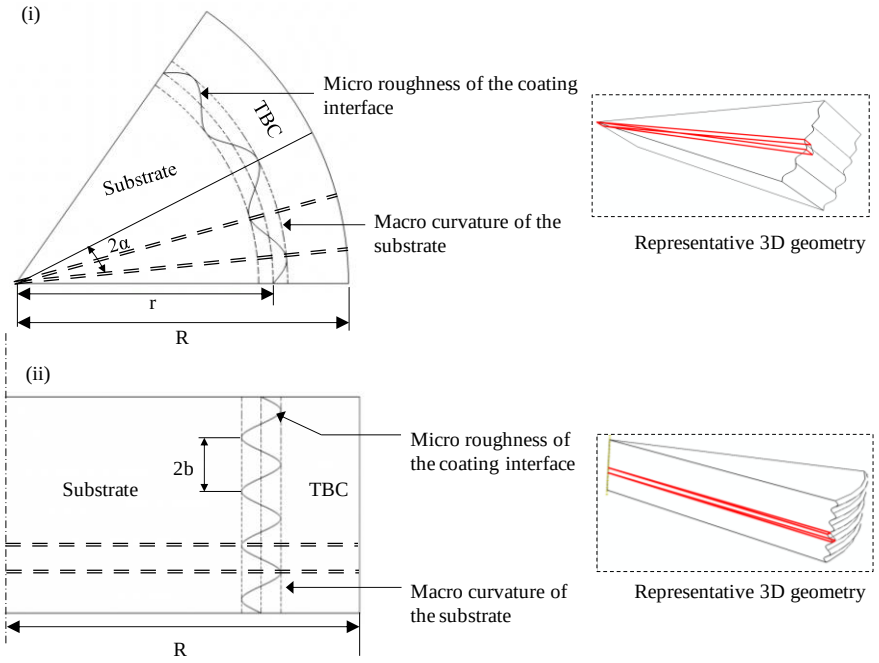

Fig.6: Sinusoidal TGO interfaces i) periodicity in the circumferential direction with wavelength of $2r\alpha$ and ii) periodicity in the longitudinal direction with wavelength of $2b$ (Cells bounded by double-dashed line are used for FE unit cells)

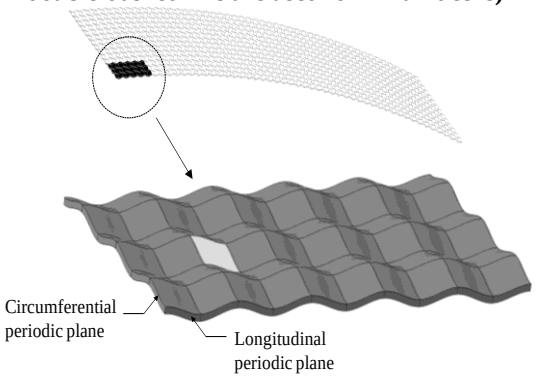

Fig.7: Representative 3D coating surface (A unit cell is highlighted)

Formatted: Font: 12 pt, Not Bold

Formatted: Font:

Formatted: Font: 12 pt, Not Bold

In principle, this unit cell involves symmetries about planes $x=\pm b$ and $\theta=\pm\alpha$. However, purely translational symmetry, such as that presented by Li and Wongsto [29] for composite structures with geometrically periodic patterns, does not properly consider the rotational aspects of the circumferential periodicity as they involve consideration of a cylindrical coordinate system (CSYS). Moreover, the commercial FE systems do not typically incorporate the ability to apply the appropriate symmetries in a cylindrical coordinate system, and do not allow the source code to be extended to incorporate such features. Accordingly, the displacements need to be transformed from a cylindrical CSYS into a rectangular one using the transformations shown in Eq (4)~~(4)~~, based on simple trigonometry:

$$\begin{aligned} u_x &= u \\ u_r &= v\cos\theta + w\sin\theta \\ u_\theta &= -v\sin\theta + w\cos\theta \end{aligned} \tag{4}$$

where u_x, u_r and u_θ are displacements in a cylindrical coordinates system (x-r-θ) and u, v and w are displacement components in a global Cartesian coordinate system (x-y-z) as shown in Fig. 8~~Fig. 8~~.

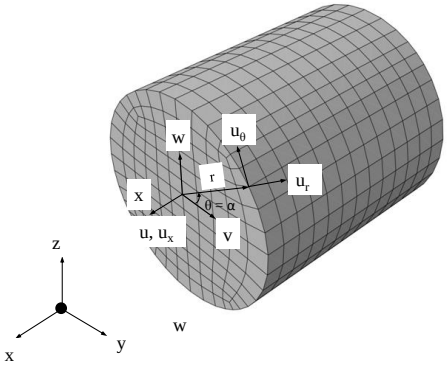

Fig. 8: Relationship between displacement components u_x, u_r and u_θ in cylindrical x-r-θ coordinate system, and displacement components u, v and w in Cartesian (x-y-z) coordinate system

Based on this transformation, Li et al. [20] extended the approach of [29] to obtain a set of boundary conditions periodic in both x and θ, of which a special case are conditions where there is symmetry about planes x=±b and θ=±α which are applied within a Cartesian CSYS. These boundary conditions for a 3D unit cell as shown in Fig.7~~Fig.7~~ (iii), for calculation of thermo-mechanical stresses, can be represented in Eq (5)~~(5)~~ [20].

$$\begin{gathered} \text{At } x = 0,\ u = 0 \\ \text{At } x = b,\ u = b\,\varepsilon_x^0 \text{; where } \varepsilon_x^0 \text{ is strain in the X-direction} \\ \text{At } \theta = 0,\ w = 0 \\ \text{At } \theta = \alpha,\ -v\sin\theta + w\cos\theta = 0 \end{gathered} \tag{5}$$

The first two boundary conditions of Eq (5)~~(5)~~ are applied to the unit cell with length, b. The boundary conditions ensure that the unit cell represents the infinitely long cylinder by constraining the plane at $x = b$ to remain parallel while allowing displacement to occur in the longitudinal direction.

Similarly, the last two boundary conditions of Eq (5)~~(5)~~ are applied for symmetry and periodicity conditions in the *r-θ* plane. In the case for which the substrate is flat, simple transverse periodicity was applied in an analogous manner to the longitudinal periodic constraints in Eq (5)~~(5)~~. By using Eq (5)~~(5)~~, it is possible to model only a quarter of the 3D unit cell, as highlighted in Fig.7~~Fig.7~~, in order to reduce computation time without affecting the accuracy of the numerical calculations.

Formatted: Font: 12 pt, Not Bold

4 FE model

Each aspect of the FE model for 3D coating interfaces is described in the following sections. The current FE model is based on the previous work by authors for 2D coating interfaces [6, 20] where details of relevant aspect of the model can be found. A case study for validation of the stresses at the coating interfaces simulated by the model against Raman and photo-stimulated luminescence piezo-spectroscopic measurements was carried out in [30]. The study showed that residual stresses predicted from the FE model is of a similar order to the stresses measured. The predictions of crack initiation and spallation sites from the model are also in agreement with experiments.

4.1 Implementation of boundary and loading conditions

Equation constraints are applied at nodes on planes of symmetry and periodic planes of the unit cell to satisfy the boundary conditions from Eq (5)~~(5)~~. In order to implement the periodic boundary conditions, a fictitious or non-structural node is defined to which the *x*-displacements of all the nodes on the boundary *x=b* are tied via linear constraint equations, with the x-displacement being made equal to the value of ε_x.

A simulated constant temperature load of 1000°C was applied across the system for a simulated time of 900 h before cooling back to room temperature. The duration of initial heating to 1000˚C from room temperature and cooling down to room temperature was 30 min. For the system with the preceding heat treatment duration of 500 h at 940°C, the thickness of the initial TGO was set as 4 μm; otherwise, the thickness was assumed to be 1 μm. However, residual stresses from earlier heat treatments were not taken into account and all systems were assumed to be stress-free at the start of the analysis.

4.2 Material properties and oxidation kinetics

For this study, the TC is assumed to be purely elastic whereas creep behaviours of other layers are considered by using a power law. A power law creep strain rate ($\dot{\varepsilon}_{ij}^{cr}$) is shown in Eq (6)~~(6)~~. Power law constants for the TGO are A_0 = 6800 $MPa^{-n}s^{-1}$, n = 2.3, Q = 4.24 x 10^5 J/mol. *Q* and *R* in Eq (6)~~(6)~~ are the activation energy of the reaction and the universal gas constant respectively. For the TC, evolution in its elastic modulus due to sintering is considered. Material properties of the BC (elastic, creep and CTE) are calculated based on its constituents that constantly vary due to oxidation or diffusion at the BC/substrate interface. The procedure is explained in Section **Error! Reference source not found.**~~4.3~~. More details can be found in an earlier publication [6].

$$\dot{\varepsilon}_{ij}^{cr} = A_0 \exp\left(-Q/RT\right)\sigma^n \quad (6)$$

It was assumed that the oxidation of the BC produces isotropic strain according to the Pilling-Bedworth Ratio (PBR) of aluminium (Al). As in the model in [27], the PBR of Al is taken to be 1.28. The oxide formed is assumed to be made up of pure alumina and it is assumed to grow towards the BC since the oxygen diffusion rate within Al_2O_3 is higher than that of Al at the same temperature [31]. The growth strain rate $\left(\dot{\varepsilon}_{ij}^{tr}\right)$ due to oxidation is related to the PBR for Al containing phases in the BC (β and γ') and the oxide formation rate $\left(\dot{f}_{ox}\right)$ via Eq (7)~~(6)~~ [5].

$$\dot{\varepsilon}_{ij}^{tr} = \frac{1}{3}\ln(PBR_{\beta/\gamma'})\,\dot{f}_{ox}\delta_{ij} \quad (7\text{~~6~~})$$

As mentioned by Taylor et al. [32], local Al-depletion zones and external growth of non-Al oxides (spinels) are expected around the oxide features with high aspect ratios such as the oxide loop. Due to their significantly higher PBR than Al, fast growing oxides of Ni, Co and Cr create a rapid increase in out-of-plane tensile stress within the TBC system during steady state heating. The failure caused by this type of metal oxidation, due to Al depletion within the BC, is referred to as 'chemical failure'. However, studying chemical failure is outside the scope of this article so therefore spinel formation due to external oxidation will not be considered here.

4.3 Modelling evolution of material properties of coatings

The high temperatures experienced by TBC systems during industrial service can cause the properties of the materials to change with time. Sintering of the ceramic TC at these temperatures can reduce the porosity of the TBC. The constitutive model which considers changes in TBC modulus due to sintering, based on the Arrhenius model, has been coupled to a FE model of the TBC system by Kyaw et al. [6]. The proportions of phases within the BC change continuously during the steady state period of heating due to oxidation or interdiffusion at the substrate/BC interface. These changes can be calculated by using finite difference (FD) calculations in combination with thermodynamic calculations such as CALPHAD [33] as presented in [34, 35]. The atomic flux of Al at the BC / TGO interface is calculated by using an empirically derived oxidation law [36]. Currently, a 1D FD/thermodynamics model developed by Karunaratne et al. [3], is coupled to the FE model of the TBC. Using the proportions of intermetallic phases predicted by the model, Eshelby's theorem and material properties of the pure BC phases, a constitutive material model was developed in [5] for the aggregate properties (elastic and creep properties and coefficient of thermal expansion (CTE)) of the BC. This model for the BC will also be adopted here.

To transfer the 1D phase proportion data into the 3D FE models, the BC was modelled as a multi-layered structure as shown in Fig.9~~Fig.9~~. The thickness of each layer was predefined at the pre-processing stage and the material points, at which the BC properties were calculated, were assumed to lie along the middle profile of each BC layer as shown in Fig.9~~Fig.9~~. Sporadically, layers of the BC were also transformed into the TGO layer based on the oxidation law in [36]. This transformation also imposes an appropriate growth strain based on the PBR of Al, to model oxidation. For the regions further away from the TGO interface, distances of material points from the TGO interface were estimated from the interface BC shown in Fig.9~~Fig.9~~. At those regions, errors in estimating distances due to the

Formatted: Font:

Formatted: Font: 12 pt, Not Bold

Formatted: Font: 12 pt, Not Bold

Formatted: Font: 12 pt, Not Bold

undulated nature of the interface are tolerable as the change in BC composition is subtle. This type of multi-layered modelling approach would also be suitable for incorporating 1D phase data into complex 3D coating tomography such as the one measured by the synchrotron-radiation method [12]

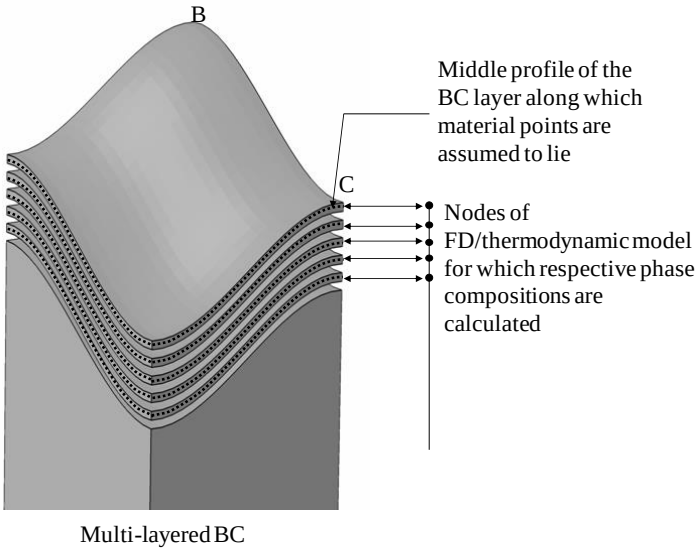

Fig.9: The multilayered nature of the BC to implement 1D FE model for the composition of the BC

4.4 Finite element mesh

It is necessary to select appropriate element types and mesh densities for the FE models with interface geometries described in Section 2.2~~2.1~~, in order to obtain accurate results with minimum computation time. For the axisymmetric models, 4-node linear axisymmetric elements (CAX4) were used for consistency with other work in the present project that makes use of ABAQUS features (XFEM and cohesive modelling) not available with higher-order elements. Reduced integration (i.e. use of fewer Gaussian integration points than are required for exact integration of the stiffness matrix) was used both for computational economy and to avoid any danger of shear locking [37].

To overcome the inaccuracies in using linear elements with a reduced integration scheme, a relatively high mesh density is necessary around the regions with abrupt changes in displacements and hence in the resultant stress and strain. For TBC systems, stress concentrations occur around the TGO interface due to CTE mismatch [38, 39] and hence, higher mesh densities were applied at those regions. A mesh diagram for the axisymmetric model (geometry set (i), Section 2.2~~2.1~~) is illustrated in [6] while mesh diagrams for geometry set (ii) and (iii) are illustrated in Fig.10~~Fig.10~~ and Fig.11~~Fig.11~~, respectively.

Formatted: Font: 12 pt, Not Bold

Formatted: Font: 12 pt, Not Bold

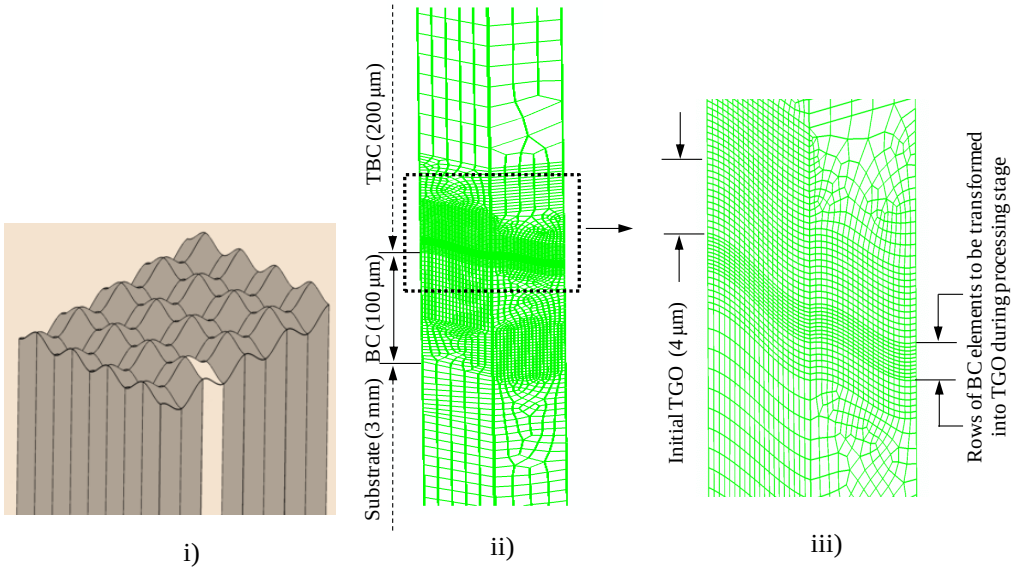

Fig.10: i) Topography of the repeated sinusoidal oxide interface with highlighted unit cell for ii) FE mesh for the unit cell iii) Detail of mesh in the vicinity of the TGO

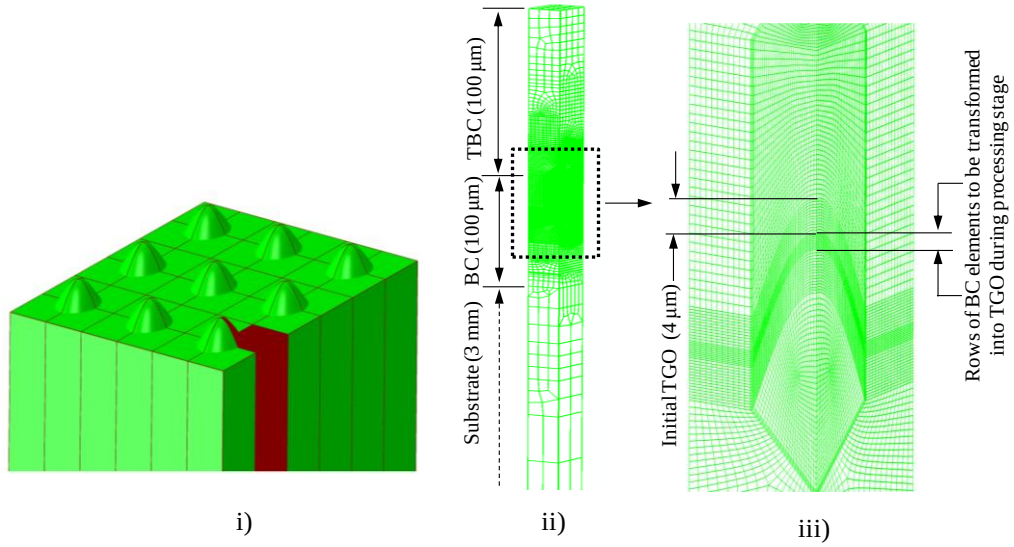

Fig.11: i) Topography of the repeated oxide loop interface with highlighted unit cell ii) FE mesh for the unit cell iii) Detail of mesh in the vicinity of the TGO

5 Results and discussions

5.1 Stresses predicted by the TBC models with axisymmetric and 3D interfaces with identical aspect ratio of geometry set i

A comparison of out-of-plane TBC stresses for both the axisymmetric and 3D models using geometry set (i), at a simulated temperature of 20°C and a simulated 900h of ageing at 1000°C, is presented in Fig.12~~Fig.12~~. It was found that when the 3D model was employed, the maximum tensile out-of-plane stresses at the TGO / TBC interface increased by a factor of nearly two. Similar findings were also presented by Gupta, et al.[18] and Glynn et al.[40]. These findings illustrate the importance of employing 3D models while carrying out stress analyses for TBC systems to avoid the underestimation of stresses caused through the use of a 2D profile.

Higher stress concentrations at the TGO / TBC interfaces for the 3D model can be explained by a simple Lamé approach as described by Gong and Clarke [41]. In such an approach, local interfacial stresses at the peak and valley regions of 2D and 3D models can be idealised as stresses at the coating interface for cylindrical and spherical substrates respectively. Analytically, it can be proved that, for an identical radius, radial stress at the coating interface for a spherical substrate is around 1.5 times higher compared to the cylindrical substrate, which is a similar magnitude to the stress differences indicated here.

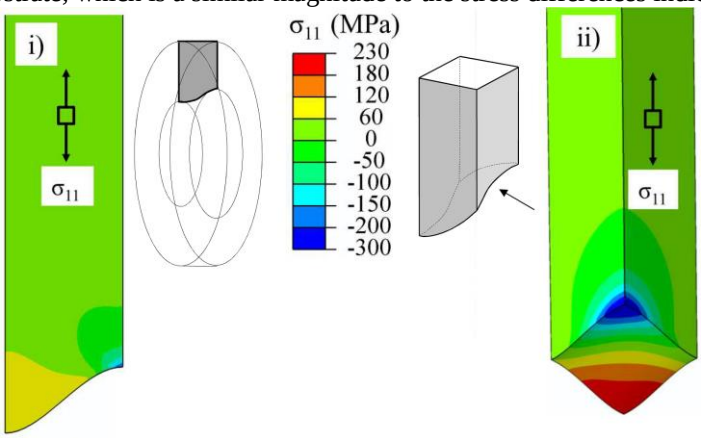

Fig.12: Out of plane tensile stress within the TBC with i) axisymmetric TGO interface and ii) 3D TGO interface at 20°C after heating at 1000°C for 900h. Insets show relationships of main views to the 3D geometry.

5.2 Stresses predicted by the TBC models with 3D sinusoidal interface (geometry set ii)

Two different simulations were carried out, both with the same interface geometry as that shown in Fig.4~~Fig.4~~. System 1 was a simulated as-sprayed system with an assumed initial TGO thickness of 1 µm. By contrast, for the simulated thermally aged sample, System 2, the initial TGO was assumed to be 4 µm thick with a fully sintered TBC after an applied heat treatment of 500 h at 960°C. Moreover, the FD / thermodynamics model for evolution of the BC material properties (Section 4.3) was also modified to ensure the initial properties of the BC were equivalent to those of an aged system. A slower oxide formation rate was also used in the simulation since diffusion of O and Al will be much slower due to the thickness of the initial TGO layer.

Firstly, the stresses within the coatings from System 1 and the idealised model from Section 5.1 were compared to investigate the significance of the coating aspect ratio. The trend of out-of-plane stresses within the TBC and the BC (shown in Fig.13~~Fig.13~~ and Fig.14~~Fig.14~~ respectively) at the end of cooling for both systems was similar despite the

Formatted: Font: 12 pt, Not Bold

Formatted: Font: 12 pt, Not Bold

Formatted: Font: 12 pt, Not Bold

Formatted: Font: 12 pt, Not Bold

unsymmetrical coating interface of System 1. Generally, out-of-plane stresses are higher than those predicted using the idealised 3D model (Fig.13~~Fig.13~~ and Fig.14~~Fig.14~~). This is due to the higher aspect ratio of the interface (0.15) compared to the ratio of the idealised 3D model (0.125). The trend of increased residual stresses within the system with increasing aspect ratio of the coating interface is similar to the one given from various 2D parametric studies [8, 28, 42] of the effect of aspect ratio on TBC stresses.

Formatted: Font: 12 pt, Not Bold

Formatted: Font: 12 pt, Not Bold

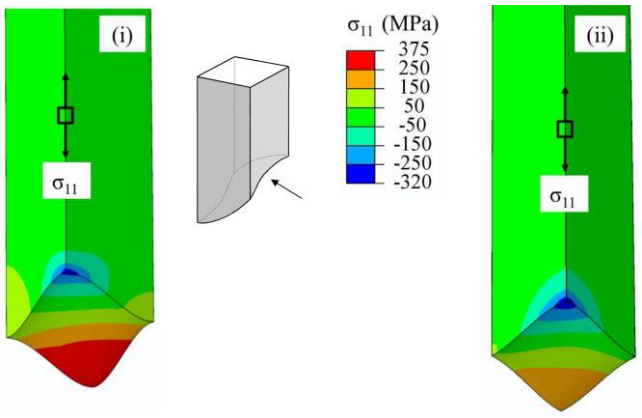

Fig.13: Through thickness stress (σ_{11}) in the vicinity of the TBC for (i) System 1 and (ii) idealised 3D interface at 20°C after heating at 1000°C for 900h. Inset shows relationships of viewing direction relative to the 3D geometry.

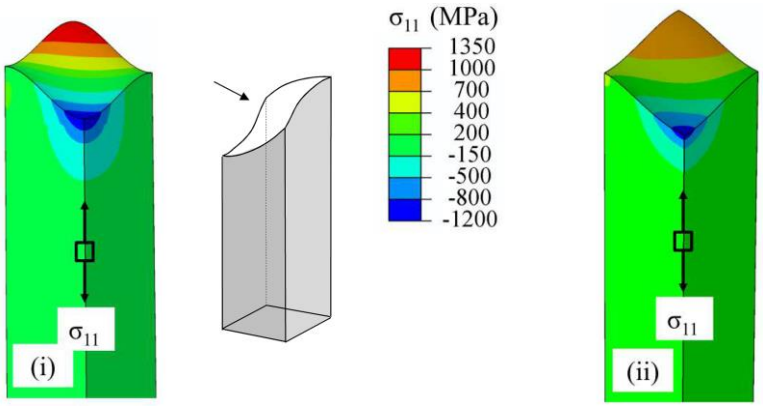

Fig.14: Through thickness stress (σ_{11}) in the vicinity of the BC for (i) system 1 and (ii) for idealised 3D interface at 20°C after heating at 1000°C for 900h. Inset shows relationships of viewing direction relative to the 3D geometry.

Secondly, stresses occurring within System 1 and System 2 were compared against each other. At the end of the heating period, both systems produced a similar out-of-plane stress pattern as shown in Fig.15~~Fig.15~~. The higher magnitude of stresses for System 2 is due to the lower strain tolerance of the aged TBC [43]. During steady state heating, lateral oxide growth imposes compressive in-plane stresses within the TGO. Concurrently, there will be additional creep strain of the TGO to relax the built-up stresses. Compressive in-plane stress

Formatted: Font: 12 pt, Not Bold

within the growing oxide layer will impose tensile and compressive out-of-plane stresses at the valleys and peaks at the TGO interfaces. These oxidation stresses are opposed to the initial thermal mismatch stresses and hence would be expected to lead eventually to stress reversal. In the case of System 1, the stress reversal occurs rapidly after heat-up as the newly-grown oxide is almost adjacent to the TBC layer. However, in the case of the heat-treated NiCoCrAlY specimen, both depletion of the Al containing phases and a thicker TGO make the oxide formation rate within the system much slower than System 1. Accordingly, the rate of change of the TBC stresses due to oxide growth is much slower, and stress reversal occurs much later as demonstrated in Fig.15~~Fig.15~~. Moreover, oxide growth stresses produced at the TBC / TGO interface during the steady state heating period for System 1 are significantly higher than those produced by System 2 at the end of the steady state heating period (Fig.15~~Fig.15~~). As a result, out of plane stresses at the TBC / TGO interface for System 1 after cooling are at least 40% higher than those predicted from System 2.

The above discrepancies in stresses between Systems 1 and 2 show the importance of using appropriate initial TGO thickness, diffusion and oxidation models whilst carrying out stress analyses on real interface geometries extracted from aged coating systems.

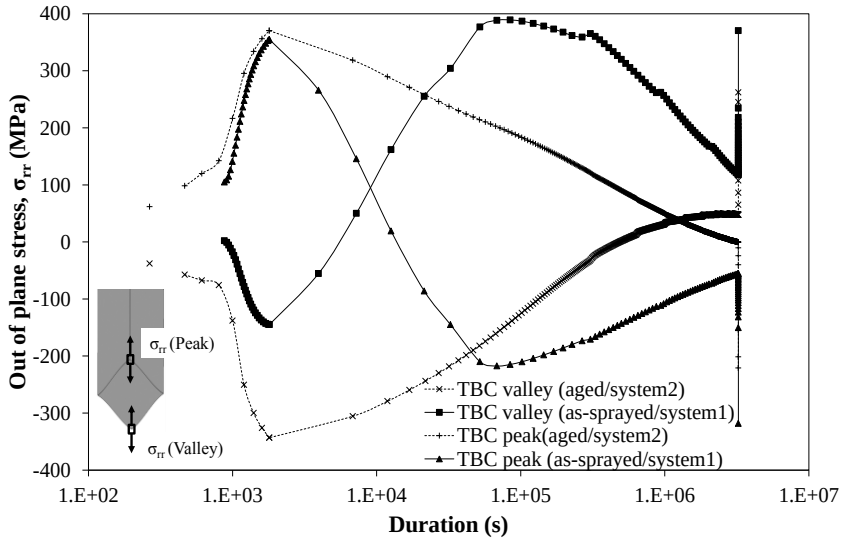

Fig.15: Out-of-plane stress at the TBC peak and valley for as-sprayed (Sample 1) and aged (Sample 2) TBC systems with an identical coating asperity

Quantitative comparisons of stresses obtained in this study against other findings in the literature pose challenges due to differences in modelling methods (e.g. with or without TGO growth strain during steady state), material properties (e.g. diffusion model for estimating instantaneous properties of the BC or fixed properties, inclusion or exclusion of creep properties of coatings) and TGO thickness. Generally, stresses predicted in this study using homogenous materials with simplified TGO interfaces are higher than those predicted from the models with actual TGO interfaces by Gupta et al. [18], and Hansson and Skogsberg [44]. From their studies with microscopically scanned 3D TGO interface, maximum through thickness TBC stress after cooling to 100˚C from 1100˚C is around 200MPa for both as-sprayed TBC system without TGO and for the system with TGO after 200h of isothermal heat treatment. The maximum stress occurs at the peak of the TBC for the as-sprayed system while it is found at the valley of the interface of the as-aged system, in a similar manner to the results obtained in the present study shown in **Fig.13**~~**Fig.13**~~ (ii). The maximum TBC stress after cooling in the present study (~ 375MPa) is higher than the magnitude of TBC stress by

Formatted: Font: 12 pt, Not Bold

Formatted: Font: 12 pt, Not Bold

Formatted: Highlight

Gupta for both as-sprayed and aged systems as shown in Fig.13~~Fig.13~~. The reason for this discrepancy could be the lack of TGO growth stress and creep within the models presented in references [18] and [44] and their assumption that the system is stress-free before cooling. Studies in references [6] and [45] have shown that the combination of TGO growth stresses, and relaxation caused by the TGO creep at the steady state, results in tensile out of plane stress at the TBC valley and these stresses further increase during cooling due to CTE mismatches between coating layers. Experimentally, hydrostatic growth stresses when the aluminium-rich BC transforms to TGO at 1121˚C have been measured to be around 2-2.5 GPa [46]. Therefore, the TBC system cannot be assumed to be stress-free before cooling, and an appropriate oxide growth model has to be used to model stresses within the system due to TGO growth during the steady state.

Formatted: Highlight

5.3 Stresses predicted by the TBC models with oxide loop geometry (geometry set iii)

Because of the convoluted geometry of the oxide loop, high tensile through-thickness stresses are predicted to be concentrated at the TBC peak at the end of heating to 1000°C, as shown in Fig.16~~Fig.16~~ (i). In reality, these stresses will be relaxed through the formation of parallel cracks or by creep of the coatings during steady state heating. Only the latter process was considered in this case. Due to stress relaxation by coating creep, tensile out-of-plane stresses at the TGO interfaces at the end of the steady state heating period are predicted to be below the rupture strengths of the interfaces. Thermal mismatch upon cooling will produce tensile out-of-plane stress at the BC peak and at the middle of the TBC / TGO interface as shown in Fig.16~~Fig.16~~ (ii). In the region where the interfacial geometry is flat, out-of-plane stresses are negligibly small although high compressive in-plane stresses of up to 6.5 GPa are created within the TGO due to cooling as shown in Fig. 17~~Fig. 17~~. Therefore, studies of both in-plane and out-of-plane stresses are necessary to predict crack growth near the coating asperities similar to the oxide loop model. Gupta et al. [18] also carried out stress analysis of the coating system using the TGO interface similar to the oxide loop in this study. By contrast, however, the feature was idealised as a hemisphere instead of the approximately conical shape in the current study. Gupta's study shows that the maximum through thickness TBC stress (~ 200MPa) occurs at the peak of the TBC after cooling for the system without TGO. When a TGO layer of 10 μm is used, the maximum TBC stress (~ 200MPa) occurs at the middle of the TBC/TGO interface in a similar manner to the current study as shown in Fig.16~~Fig.16~~. As mentioned previously, TBC stresses at the end of heating (shown in Fig.16~~Fig.16~~ (i)) will be redistributed during steady state due to relaxation caused by TGO creep and due to TGO growth. Neither of these processes was considered in the Gupta model and hence the magnitude of stress is not directly comparable with the present study.

Formatted: Font: 12 pt, Not Bold

Formatted: Font: 12 pt, Not Bold

Formatted: Font: 12 pt, Not Bold, Highlight

Formatted: Font: 12 pt, Not Bold, Highlight

Comment [JA1]: Presumably this is what you mean – original wording was ambiguous

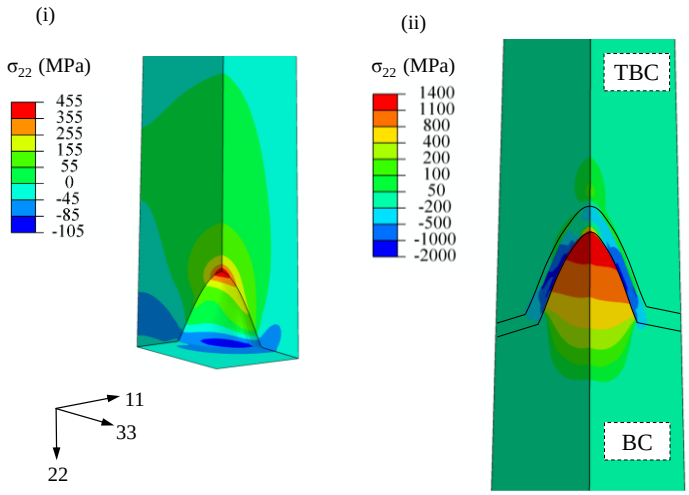

Fig.16: Through thickness stresses (i) within the TBC at the end of heating at 1000°C and (ii) within the TBC system near the TGO interfaces at the end of cooling after heating at 1000°C for 900h

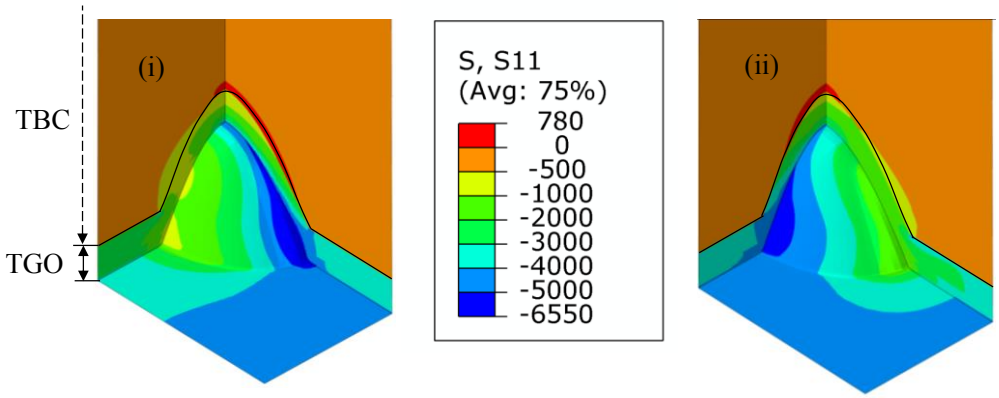

Fig. 17: In-plane stress (i) S11 and (ii) S33 within TGO and TBC at the end of cooling after heating at 1000°C for 900h

5.4 Prediction of crack development and failure of the TBC system based on stress distributions within the system

In this paper, crack initiation and subsequent propagation are not modelled but they are rather predicted from out of plane tensile stress state (assuming that the coating is brittle and mode I crack growth is the dominant fracture mode). When the axisymmetric interface with geometry set (i) is considered, propagation of parallel cracks due to residual stresses at three different stages during a thermal cycle can be predicted as shown in Fig.18~~Fig.18~~. Parallel cracks around the TBC peak towards the TBC valley after the heating period, are restricted due to the high compressive stress at the valley as shown in Fig.18~~Fig.18~~ (i). However for aged systems, reversal of tensile and compressive stresses is only predicted to occur after several hours of steady state heating (Fig.15~~Fig.15~~) and parallel cracks formed at the TBC peak during heat-up will continue to propagate. Therefore, premature spallation of

Formatted: Font: 12 pt, Not Bold, English (U.S.)

Formatted: Font: 12 pt, Not Bold, English (U.S.)

Formatted: Font: Not Bold

the TBC is expected for thermally aged systems. During steady state heating, additional parallel cracks are expected to nucleate at the TBC valley due to stress reversal at the TBC peak and valley as shown in Fig.18~~Fig.18~~ (ii). When cooling is applied, any CTE mismatch is predicted to cause tensile out-of-plane stresses in the vicinity of the peak of BC and the valley and slope of the TBC as depicted in Fig.18~~Fig.18~~ (iii). Therefore, parallel cracks are expected to form at those regions. Formation of parallel cracks at the BC peak, however, is not possible due to its high tensile strength [47] at low temperature. Delamination or interfacial cracks are also expected to form at the BC / TGO interface because of higher out-of-plane tensile stresses compared to those at the TGO / TBC interface. If delamination does occur, the strain energy release from interfacial cracking could drive further propagation of existing TBC and TGO cracks.

The above predictions of possible parallel crack formations at different stages of a thermal cycle based on radial stresses within the system (Fig.18~~Fig.18~~) can be schematised as shown in Fig.19~~Fig.19~~.

Similarly, local crack growth in the vicinity of 3D asperities based on out-of-plane tensile stresses obtained from stress analyses could occur except when significant regions of the interface are flat. In this case, very high compressive in-plane stresses are expected and buckling-driven cracks have to be considered. Buckling is favoured especially if there are significant de-cohesion zones at the interface [48]. For a flat interface shown in Fig.20~~Fig.20~~, the minimum compressive stress for initiation of buckling failure, is directly proportional to the thickness of the coatings (h) and inversely proportional to the temperature changes (ΔT) and half of the length of interfacial de-cohesion (b), according to the analytical derivation by Choi et al. [49]. For the oxide loop model (Fig.11~~Fig.11~~), expected buckling zones, along with parallel cracks formed from out-of-plane tensile stresses at the end of cooling, are illustrated in Fig.21~~Fig.21~~.

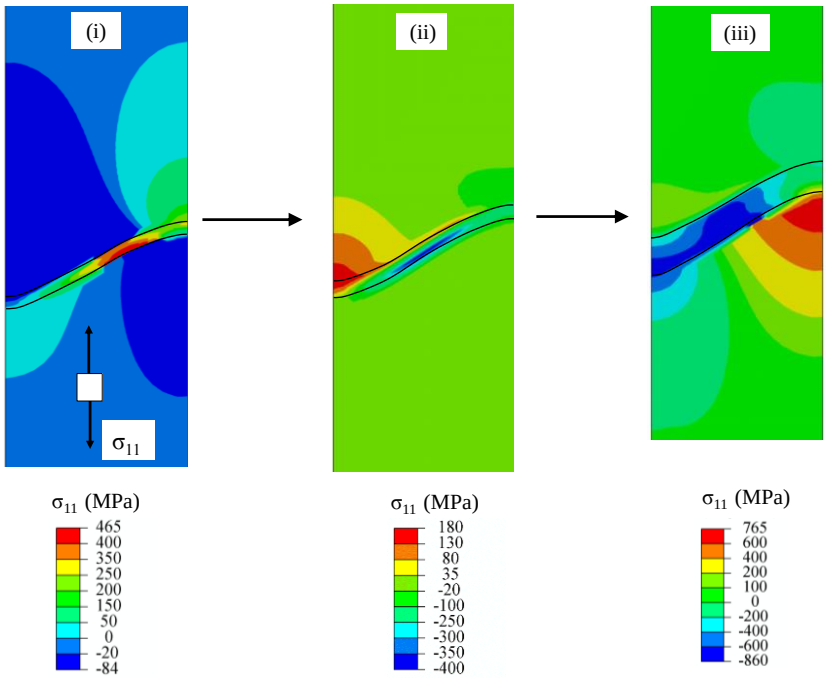

Formatted: Font: 12 pt, Not Bold, English (U.S.)

Formatted: Font: 12 pt, Not Bold, English (U.S.)

Formatted: Font: 12 pt, Not Bold, English (U.S.)

Formatted: Font: 12 pt, Not Bold, English (U.S.)

Formatted: Font: 12 pt, Not Bold

Formatted: Font: Not Bold

Formatted: Font: Not Bold

Fig.18: Through thickness stress state (σ_{11}) within the TBC system with axisymmetric TGO interface at (i) at the end of heating (ii) after heating at 1000°C for 13h (iii) at 20°C after heating at 1000°C for 90h

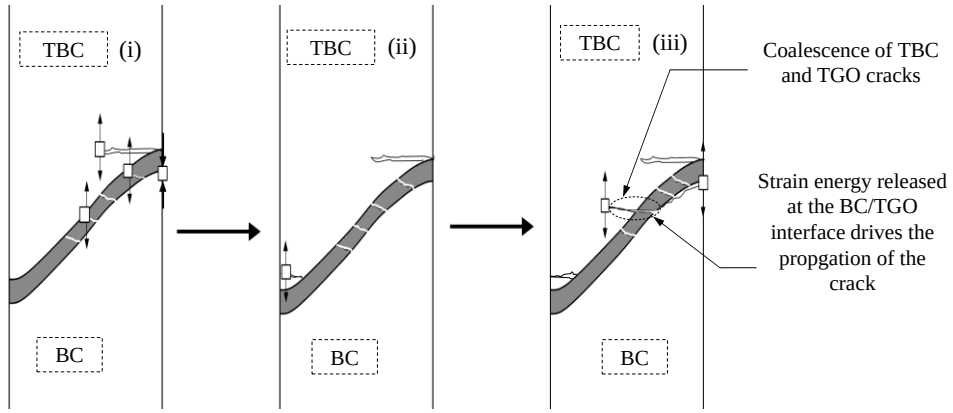

Fig.19: Stages of predicted crack growths within the TBC system with axisymmetric TGO interface relating to stress states shown in Fig.18~~Fig.18~~ (Note: Aspect ratio of the TGO interface is exaggerated)

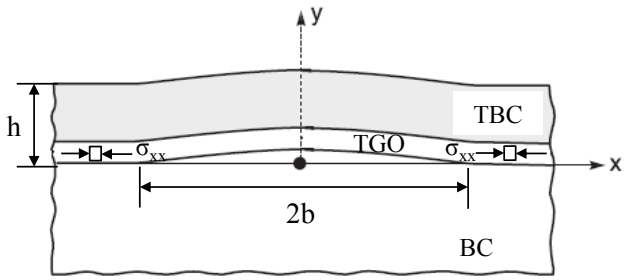

Fig.20: Schematic diagram of interfacial decohesion at the flat TGO/BC interface

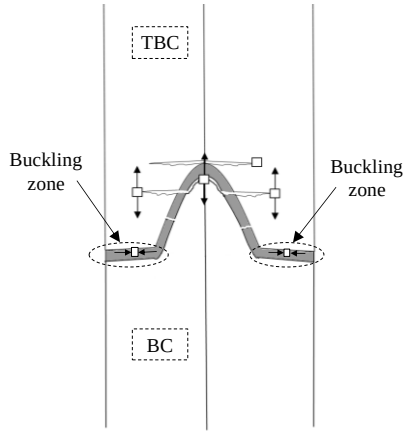

Fig.21: Predicted crack growth within the oxide loop model at the end of cooling

6 Conclusions

The following conclusions can be made from the stress analyses presented in this paper.

- For identical aspect ratios, the maximum compressive and tensile radial stresses at the TBC / TGO interface of the 3D model are around twice the values predicted using the axisymmetric (2D) model. The finding is consistent with analytical results [41], which show an increase of more than 1.5 times in tensile radial stress for a spherical interface compared to a cylindrical one.
- For all geometries of the coating interface chosen in this paper, tensile stresses are predicted to be concentrated at the TBC peak and the opening of cracks is expected at the end of the heating period. The stresses near these cracks relax while their propagation towards the valley region is opposed by high compressive stress.
- After the heating stage, stress reversal at the TBC peak and valley regions does not occur rapidly for the aged system with thick initial TGOs compared to the as-sprayed system. Therefore cracks that nucleate at the TBC peak during heating continue to propagate during the steady state heating stage for aged systems and premature spallation is expected.
- At the end of cooling, tensile delamination cracks are expected to occur at the peak of the TGO / BC interface especially for the oxide loop asperity due to its high aspect ratio. Once the interface has delaminated, strain energy stored during the steady state period will be released. If coalescence of TBC and TGO cracks also occurs in the vicinity of the interfacial crack opening, strain energy release at the interface may drive further crack propagation leading to spallation.
- Additionally, buckling failure is expected for relatively flat coating interface regions due to the high in-plane compressive stresses, which occur at the end of cooling as observed from the oxide loop model.

This paper presents stress analyses within TBC systems using different unit cells of coating asperities, by assuming the coating surface is covered with an infinite tessellation of

identical asperities. However, in reality, the coating surface has several irregular microscopic features. Nevertheless, the presented framework, for setting up FE models of TBC systems, with 3D microscopic features, can be applied with future studies to explore the influence of different geometries of asperities on coating failure.

Acknowledgement

We would like to acknowledge the support of The Energy Programme, which is a Research Councils UK cross council initiative led by EPSRC and contributed to by ESRC, NERC, BBSRC and STFC, and specifically the Supergen initiative (Grants GR / S86334 / 01 and EP / F029748) and the following companies; Alstom Power Ltd., Doosan Power, E.ON, National Physical Laboratory, Praxair Surface Technologies Ltd, QinetiQ, Rolls-Royce plc, RWE npower, Siemens Industrial Turbomachinery Ltd. and Tata Steel, for their valuable contributions to the project.

Reference

[1] Wigren J, Pejryd L. Thermal barrier coatings-why, how, where and where to. 15th International Thermal Spray Conference: Thermal Spray Meeting the Challenges of the 21st Century. 1998:pp. 1531–42.

[2] Liu YZ, Zheng SJ, Zhu YL, Wei H, Ma XL. Microstructural evolution at interfaces of thermal barrier coatings during isothermal oxidation. Journal of the European Ceramic Society. 2016;36:1765-74.

[3] Karunaratne MSA, Ogden SL, Kenny SD, Thomson RC. A multicomponent diffusion model for prediction of microstructural evolution in coated Ni based superalloy systems. Maters Sci & Tech. 2009; Volume 25:287-99.

[4] Elsaß M, Frommherz M, Scholz A, Oechsner M. Interdiffusion in MCrAlY coated nickel-base superalloys. Surface and Coatings Technology. 2016;307, Part A:565-73.

[5] Hermosilla U. Mechanical modelling of thermal barrier coatings at high temperatures. University of Nottingham. Thesis (PhD), 2008.

[6] Kyaw ST, Jones IA, Hyde TH. Predicting failure within TBC system: Finite element simulation of stress within TBC system as affected by sintering of APS TBC, geometry of substrate and creep of TGO. Eng Fail Anal. 2013;27:150-64.

[7] Ahrens M, Vaßen R, Stöver D. Stress distributions in plasma-sprayed thermal barrier coatings as a function of interface roughness and oxide scale thickness. Surface and Coatings Technology. 2002;161:26-35.

[8] Hsueh CH, Fuller Jr ER. Residual stresses in thermal barrier coatings: effects of interface asperity curvature/height and oxide thickness. Materials Science and Engineering: A. 2000;283:46-55.

[9] Pindera JM, Aboudi J, Arnold SM. The effect of interface roughness and oxide film thickness on the inelastic response of thermal barrier coatings to thermal cycling. Materials Science and Engineering: A. 2000;284:158-75.

[10] Wang L, Li DC, Yang JS, Shao F, Zhong XH, Zhao HY, et al. Modeling of thermal properties and failure of thermal barrier coatings with the use of finite element methods: A review. Journal of the European Ceramic Society. 2016;36:1313-31.

[11] Asadizanjani N. 3D Imaging and Investigation of Failure and Deformation in Thermal Barrier Coatings Using Computed X-ray Tomography 2014.

[12] Maurel V, Helfen L, N'Guyen F, Koster A, Di Michiel M, Baumbach T, et al. Three-dimensional investigation of thermal barrier coatings by synchrotron-radiation computed laminography. Scripta Materialia. 2012;66:471-4.

[13] Reid ACE, Lua RC, García RE, Coffman VR, Langer SA. Modelling Microstructures with OOF2 Int J Materials and Product Technology. 2009 Vol. 35.

[14] Wang Z, Kulkarni A, Deshpande S, Nakamura T, Herman H. Effects of pores and interfaces on effective properties of plasma sprayed zirconia coatings. Acta Materialia. 2003;51:5319-34.

[15] Rezvani Rad M, Farrahi GH, Azadi M, Ghodrati M. Stress analysis of thermal barrier coating system subjected to out-of-phase thermo-mechanical loadings considering roughness and porosity effect. Surface and Coatings Technology. 2015;262:77-86.

[16] Nayebpashaee N, Seyedein SH, Aboutalebi MR, Sarpoolaky H, Hadavi SMM. Finite element simulation of residual stress and failure mechanism in plasma sprayed thermal barrier coatings using actual microstructure as the representative volume. Surface and Coatings Technology. 2016;291:103-14.

[17] Gupta M, Eriksson R, Sand U, Nylén P. A diffusion-based oxide layer growth model using real interface roughness in thermal barrier coatings for lifetime assessment. Surface and Coatings Technology. 2015;271:181-91.

[18] Gupta M, Skogsberg K, Nylén P. Influence of Topcoat-Bondcoat Interface Roughness on Stresses and Lifetime in Thermal Barrier Coatings. Journal of Thermal Spray Technology. 2014;23:170-81.

[19] Saucedo-Mora L, Marrow TJ. FEMME: A multi-scale Finite Element Microstructure MEshfree fracture model for quasi-brittle materials with complex microstructures. Engineering Fracture Mechanics. 2015;147:355-72.

[20] Li SG, Kyaw S, Jones A. Boundary conditions resulting from cylindrical and longitudinal periodicities. Comput Struct. 2014;133:122-30.

[21] Korsunsky AM, Geoffrey Gibson A, Nguyen GD, Sebastiani M, Song X, Sui T. Editorial note — On the aims & scope and priority areas in Materials & Design. Materials & Design. 2015;88:1377-80.

[22] Sohn YH, Kim JH, Jordan EH, Gell M. Thermal cycling of EB-PVD/MCrAlY thermal barrier coatings: I. Microstructural development and spallation mechanisms. Surface and Coatings Technology. 2001;146–147:70-8.

[23] FOGALE-NANOTECH. http://wwwfogalefr/optical_profilers/pages/softwarephp. 2008.

Formatted: German (Germany)

Formatted: Italian (Italy)

[24] ISO 11562. Geometrical product specification (GPS)—surface texture: profile method—metrological characteristics of phase correct filters. Geneva: International Organization for Standardization. 1996.

[25] Raja J, Muralikrishnan B, Fu S. Recent advances in separation of roughness, waviness and form. Precis Eng. 2002;26:222-35.

[26] Muralikrishnan B, Raja J. Computational Surface and Roundness Metrology. 2008.

[27] Busso EP, Evans HE, Qian ZQ, Taylor MP. Effects of breakaway oxidation on local stresses in thermal barrier coatings. Acta Materialia. 2010;58:1242-51.

[28] Ranjbar-Far M, Absi J, Mariaux G, Dubois F. Simulation of the effect of material properties and interface roughness on the stress distribution in thermal barrier coatings using finite element method. Mater & Des. 2010;31:772-81.

[29] Li S, Wongsto A. Unit cells for micromechanical analyses of particle-reinforced composites. Mech Mater 2004;36:543-72.

[30] Liu D, Kyaw ST, Flewitt PEJ, Seraffon M, Simms NJ, Pavier M, et al. Residual stresses in environmental and thermal barrier coatings on curved superalloy substrates: Experimental measurements and modelling. Materials Science and Engineering: A. 2014;606:117-26.

[31] Kofstad P. High-temperature oxidation of metals. Wiley. 1966.

[32] Taylor MP, Pragnell WM, Evans HE. The influence of bond coat surface roughness on chemical failure and delamination in TBC systems. Materials and Corrosion. 2008;59:508-13.

[33] Davies RH, Dinsdale AT, Gisby JA, Robinson JAJ, Martin: SM. CALPHAD, 2002, 26, (2), 229-271.

[34] Evans HE, Taylor MP. Diffusion Cells and Chemical Failure of MCrAlY Bond Coats in Thermal-Barrier Coating Systems. Oxidation of Metals. 2001;55:17-34.

[35] C.Che, G.Q.Wu, H.Y.Qi, and ZH, X.G.Yang. Depletion Model of Aluminum in Bond Coat for Plasma-Sprayed Thermal Barrier Coatings. Advanced Materials Research June, 2009;(Volume 75):31-5.

[36] S. M. Meier, Nissley DM, Sheffler: KD. 'Thermal barrier coating life prediction model development', Phase II Final Report. Technical Report NASA Contractor Report 18911/NAS3-23944, National Aeronautics and Space Administration, NASA Lewis Research Center, 1991.

[37] Sharma C. Displacement/mixed finite element formulation for beam and frame problems. Master Thesis (University of Pavia). 2007.

[38] Bäker M, Fiedler T, Rösler J. Stress evolution in thermal barrier coatings for rocket engine applications. Mechanics of Advanced Materials and Modern Processes. 2015;1:5.

[39] Evans AG. Mechanisms controlling the durability of thermal barrier coatings. Progress in Materials Science. 2001;46:505-53.

[40] M.L.Glynn, K.T.Ramesh, P.K.Wright, K.J.Hemker. Modelling effects of material properties and three-dimensional surface roughness on thermal barrier coatings. Mat Res Soc Symp Proc Vol 645E. 2001.

[41] X.Y.Gong, D.R.Clarke. On the Measurement of Strain in Coatings Formed on a Wrinkled Elastic Substrate. Oxid Met 1998;50:355-76.

[42] Martena M, Botto D, Fino P, Sabbadini S, Gola MM, Badini C. Modelling of TBC system failure: Stress distribution as a function of TGO thickness and thermal expansion mismatch. Eng Fail Anal. 2006;13:409-26.

[43] Thompson.J.A, Ji.W, Klocker.T, Clyne T.W. Sintering of the top coat in thermal spray TBC systems under service conditions. Ninth International Symposium on Superalloys. 2000:685-92.

[44] Hansson T, Skogsberg K. Comparison of stress behaviour in thermal barrier coatings using FE analyses (Masters thesis) University West, Sweden. 2012.

[45] Busso EP, Qian ZQ, Taylor MP, Evans HE. The influence of bondcoat and topcoat mechanical properties on stress development in thermal barrier coating systems. Acta Materialia. 2009;57:2349-61.

[46] Patel NV. Use of Thermally Grown Oxide Stress Measurements to Predict Remaining Life of Thermal Barrier Coatings under Realistic Turbine Engine Conditions (Master Thesis). University of Connecticut. 2014.

[47] R.W.Smith. Mechanical properties of a low-pressure-plasma- applied Co-Cr-Al-Y coating. Thin Solid Films. 1981;84:59-72.

[48] Timoshenko S. 'Theory of Elastic Stability'. McGraw-Hill, New York. 1936:p 367.

[49] Choi SR, Hutchinson JW, Evans AG. Delamination of multilayer thermal barrier coatings. Mechanics of Materials. 1999;31:431-47.